Fourier analysis of light scattered by elongated scatterers

Zeev Schiffer, Yosef Ashkenazy, Reuven Tirosh, and Mordechai Deutsch

Biological stimulation of living cells is sometimes associated with morphological changes. A practical method is developed to monitor cell stimulation by means of their conformational changes through interpretation of the pattern of light scattered from a cell population. For this purpose a mathematical model is suggested that predicts the power spectrum from a population of elliptic objects with a given eccentricity. A computer simulation of that model is presented together with supporting experimental results of the simulation. The predicted and the measured spectra are in good agreement. This technique was applied to elongated cells that become circular on exposure to a human hormone, indicating the potential applicability of the method in biology and medicine. The method and the apparatus presented in this study could be applied to bioassays of cell systems that respond to a variety of stimulants and to trace quantitatively the structural changes that occur during biological processes.

OCIS codes: 000.1430, 070.4790, 100.3190, 170.1530, 260.1960, 290.5820.

1. Introduction

The analysis of light scattered by small round particles is a powerful tool for determining important parameters, such as size and structure, within a given population. A very simple description of the scattering intensity is available[1–3] when the suspending media has an index of refraction close to that of the particles, such as for living cells suspended in a buffered saline solution. This is exploited in flow-through system measurements, characterizing each particular cell by its forward- and side-scattering intensities.[2,3]

A detailed analysis of the scattering pattern (differential light scattering) from a single cell was described in previous studies.[4–7] With an optical microscope that collects the light in the Fourier plane, the size and structure of a single cell is determined by means of a particular inverse Fourier transform.

However, using such a transform to determine the structural parameters of an entire cell population has not been previously attempted to our knowledge, despite the marked success of the method in other fields, such as in powder sizing and aggregate analysis.[8,9] This may be because in many cases cells have irregular shapes, and no convenient theory has been available for determining the structural parameters of such shapes. Although a few studies obtained analytical expressions for scattering by nonspherical objects,[9,10] the actual determination of the structural parameters was hindered by the complexity of the method.

The present study examines Fourier analysis of the light diffraction pattern of a randomly oriented population of homogeneous nonspherical objects. The mathematical formulation of the problem is given in terms of the spatial spectra expected from such a population. A computer simulation of a scattering experiment was performed to validate the theoretical expressions developed in this study. Experimental spectra of round and elongated biological cells are both presented.

2. Theory

A. Background: Scatter from a Flat, Round Object

Fourier analysis of differential light scattering[11] is a powerful method that is commonly used for sizing optically well-defined, spherical objects. This study expands the use of Fourier analysis to monitor oval cells measured after sedimentation on a microscopic slide, which flattens them. For the sake of clarity we first explain the basic principles of optical sizing by briefly reviewing the case of spherical cells.

A living cell has on the average, a refractive index that is only slightly greater than its suspending, wa-

The authors are with the Jerome Schottenstein Cellscan Center for Early Detection of Cancer, Department of Physics, Bar-Ilan University, Ramat-Gan 52900, Israel. M. Deutsch's e-mail addresses are m_d@netvision.net.il and arnon-sh@actcom.co.il.

Received 6 November 1998; revised manuscript received 5 March 1999.

0003-6935/99/163626-10$15.00/0

terlike solution media, e.g., phosphate-buffered saline. Its diameter of a few micrometers is much larger than the incident radiation wavelength (e.g., for a He–Ne laser, $\lambda = 0.633$ μm). Thus

$$(T/\lambda)\Delta n < 1, \tag{1}$$

$$\lambda/D \ll 1, \tag{2}$$

where T is the thickness of a cell sedimented onto a glass slide before measurement, Δn is the difference between the indices of refraction of the object and the suspending media, and D is the typical diameter of the measured cell.

The physical meaning of inequality (1) is that the phase accumulation of a wave passing through such a scatterer will be less than one complete cycle, whereas that of inequality (2) is that the scattering pattern will be concentrated in the forward direction. In such cases the intensity pattern $I(\theta, \phi)$ of the light scattered by the cell is given by the Fraunhofer diffraction approximation,[12]

$$I(\theta, \phi) = \frac{\beta}{2}\left|\int_{-\infty}^{\infty}\int_{-\infty}^{\infty} T(x, y)\exp[iK(x \sin\theta + y \sin\phi)]\mathrm{d}x\mathrm{d}y\right|^2, \tag{3}$$

where K is the wave number $(2\pi/\lambda)$ of the incident radiation; $T(x, y)$ is the aperture function, which is the thickness of the object at a point (x, y); and the angles (θ, ϕ) are the scattering angles relative to the x' and y' scattering axes. Thus, $K(x \sin\theta + y \sin\phi)$ is the phase difference between a ray scattered from a given point (x, y) in the object plane and a ray scattered from an arbitrary origin $(x = y = 0)$. Both scattered rays impinge upon the detector and would be set at the angles θ and ϕ as shown in Fig. 1. The definition of β is discussed below. In the regime where Eq. (3) is valid, it can be shown[12] that $\phi, \theta \leq (0.6\lambda/T)^{1/2}$. Therefore, for a cell thickness of ~5 μm, one has $\phi, \theta \leq (0.6 \times 0.1)^{1/2} \approx 0.25$ rad. Thus $\sin\theta \approx \theta$, $\sin\phi \approx \phi$, and Eq. (3) is reduced to

$$I(\theta, \phi) = \frac{1}{2}\beta\bar{T}^2\left|\iint_S \exp[iK(x\theta + y\phi)]\mathrm{d}x\mathrm{d}y\right|^2, \tag{4}$$

where a mean thickness $\bar{T}$ of a flattened object is assumed and integration is performed over the region S, defined by the boundaries of the object.

For cells with a circular boundary, integration of Eq. (4) yields

$$I(\theta, \phi) = 2\beta(\bar{T}\pi R^2)^2\left\{\frac{J_1[KR(\theta^2 + \phi^2)^{1/2}]}{KR(\theta^2 + \phi^2)^{1/2}}\right\}^2 = 2\beta(V_{\mathrm{cell}})^2\left\{\frac{[J_1[KR(\theta^2 + \phi^2)^{1/2}]}{KR(\theta^2 + \phi^2)^{1/2}}\right\}^2, \tag{5}$$

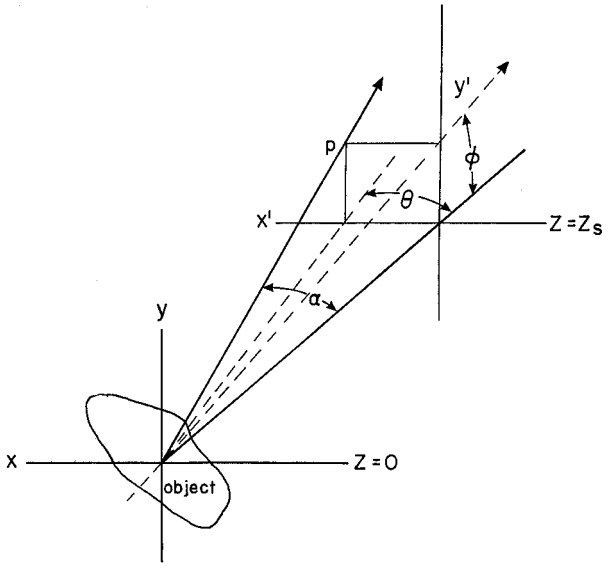

Fig. 1. Scattering and diffraction planes. The scattering object is defined in the xy plane ($Z = 0$). A scattering pattern is created at the diffraction plane $x'y'$ ($Z = Z_S$) with each representative point p also defined by the scattering azimuthal angles; $Z_S \gg r_{\max}$. (The scatterer dimension is exaggerated for illustrative purposes; $\sin\theta \cong \theta$, $\sin\phi \sim \phi$.)

where R is the cell radius, $V_{\mathrm{cell}} = \bar{T}\pi R^2$ is the flattened cell volume, and J_1 is the first-order Bessel function of the first kind.

The definition of β can be deduced by a comparison. Each of the m radiating dipoles possesses an electric field of strength ϵ. For fully constructive interference, the resultant electric field is given by

$$E = m\epsilon,$$

and the corresponding intensity is

$$I = 1/2m^2\epsilon^2,$$

that is, the square of the number of sources (m^2) multiplied by the square of their individual electric fields. Similarly, in the case of fully constructive interference scattering in the forward direction, the number n of dipole sources in a cell is proportional to its volume, $V_{\mathrm{cell}} = \bar{T}\pi R^2$. Thus I is $2\beta V^2 \propto \beta m^2 \propto m^2\epsilon^2$ with $\beta \propto \epsilon^2$, the square of the scattered electric field strength per unit volume measured at a given distance from the scatterer.

In accordance with inequalities (1) and (2) and $KR(\theta^2 + \phi^2)^{1/2} \equiv W > 1$, and within the limitations of the experimentally preselected scanning angular range of the diffracted pattern, $J_1(W)$ can be approximated by[6]

$$J_1(W) \cong \left(\frac{2}{\pi W}\right)^{1/2}\left[\cos\left(\frac{W - 3\pi}{4}\right)\right], \tag{6}$$

and therefore

$$J_1^2(W) = \frac{2}{\pi W}\cos^2\left(W - \frac{3\pi}{4}\right) = \frac{1}{\pi W}(1 - \sin 2W). \tag{7}$$

Restoring $W = KR(\theta^2 + \phi^2)^{1/2}$ and inserting Eq. (7) into Eq. (5) yields

$$I(\theta, \phi) = \frac{2\beta {V_{\text{cell}}}^2}{\pi} \frac{1 - \sin[2KR(\theta^2 + \phi^2)^{1/2}]}{[KR(\theta^2 + \phi^2)^{1/2}]^3}, \quad (8)$$

which is an approximate expression of the scattered diffraction pattern intensity produced by a flat, round cell.

B. Spatial Spectrum from a Randomly Located Population of Nonhomogeneous Round Objects

A common method for experimentally obtaining the size of a single illuminated round object is operating on $I(\theta, \phi)$, in Eq. (8), with a weighted Fourier transform, namely,

$$I(\omega) = \Im\{I(\alpha)(K\alpha)^3\} = \left| \int_{-\infty}^{\infty} I(\alpha)(K\alpha)^3 \exp(i\omega\alpha) d\alpha \right|, \quad (9)$$

where $\alpha \equiv (\theta^2 + \phi^2)^{1/2}$ is the scattering angle illustrated in Fig. 1. We use this weighted Fourier transform at a later stage [Eq. (21)], which is the primary reason for dealing with a nonhomogeneous scattering population here. Inserting Eq. (8) into Eq. (9) gives us

$$I(\omega) = \left| \int_{-\infty}^{\infty} R[1 - \sin(2KR\alpha)]\exp(i\omega\alpha) d\alpha \right| = [2\delta(\omega) + \delta(\omega - 2KR) + \delta(\omega + 2KR)]R, \quad (10)$$

where, for simplicity, the constant $2\beta {V_{\text{cell}}}^2/\pi$ is omitted. Equation (10) is a sum of three delta functions at the spatial frequencies $\omega = 0$ and $\omega = \pm 2KR$, where the latter frequencies explicitly express the size of the scatterer.

The spatial spectrum, which is the transformed scattering pattern intensity $II(\omega)$ created by homogeneous, noninteracting, and randomly located particles, can be shown to be merely N multiplied by the spatial spectrum $I(\omega)$, created by a single particle[13]:

$$II(\omega) \propto NI(\omega). \quad (11)$$

When the object size of the population under investigation is nonhomogeneous, a normalized distribution function $\rho(r)$ must be introduced, and relation (11) should then be rewritten by use of Eq. (10):

$$II(\omega) = \int_0^{r=R_{\max}} \left| \int_{-\infty}^{\infty} r[1 - \sin(2Kr\alpha)]\rho(r) \times \exp(i\omega\alpha) d\alpha \right| dr. \quad (12)$$

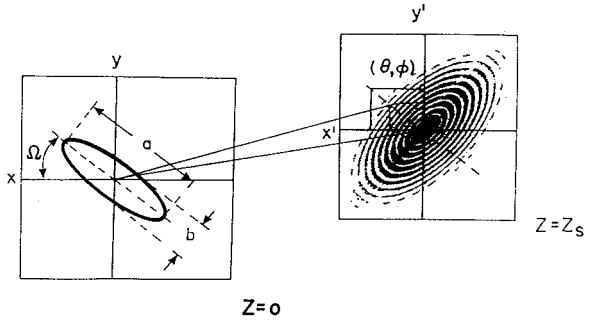

Fig. 2. Diffraction pattern created at the plane $Z = Z_S$ by an elliptic scatterer located at the object plane $Z = 0$. The density of the diffraction fringes is highest in the direction parallel to the major axis of the scattering ellipse.

Integrating over α gives us

$$II(\omega) = \int_0^{r=R_{\max}} [2\delta(\omega) + \delta(\omega - 2Kr) + \delta(\omega + 2Kr)]\rho(r) r dr. \quad (13)$$

The integral in Eq. (13) is nonzero only for $\omega = 0$ and for $r = \pm(\omega/2K)$. Considering only values of $\omega \geq 0$, one gets

$$II(\omega) = 2\delta(\omega) \int_0^{r=R_{\max}} r\rho(r) dr + \rho(\omega/2K)\omega/2K. \quad (14)$$

The second term on the right-hand side of Eq. (14) is identical to the scaled weighted distribution function $\rho(r)$, and the first term is identified as the mean radius $\bar{R}$, which multiplies a delta function at zero frequency.

C. Spatial Spectrum of a Randomly Oriented Population of Homogeneous Elliptical Scatterers

The analytical determination of structural parameters of elliptic scatterer populations requires finding an expression, $I(\theta, \phi)$, for the diffraction pattern of a single elliptic scatterer. This is accomplished with the same considerations as in Subsection 2.A, yielding Eq. (4), where the scatterer functions $T_{\text{ell}}(x, y)$ describe an ellipse. A change of the limits of integration is required in Eq. (4), as follows:

$$I(\theta, \phi) = \frac{1}{2} \beta {\bar{T}_{\text{ell}}}^2 \left| \int_{x_1=-a}^{x_2=+a} \int_{y_1=-b[1-(x/a)^2]^{1/2}}^{y_2=+b[1-(x/a)^2]^{1/2}} \exp[iK(x\theta + y\phi)] dx dy \right|^2, \quad (15)$$

where a and b are the principal axes of the ellipse as shown in Fig. 2.

Integrating Eq. (15) with respect to y yields

$$I(\theta, \phi) = \frac{1}{2}\beta\bar{T}^2\left|\frac{2}{K\phi}\int_{x_1=-a}^{x_2=+a}\sin\left\{Kb\phi\left[1-\left(\frac{x}{a}\right)^2\right]^{1/2}\right\} \times \exp(iKx\theta)\mathrm{d}x\right|^2. \quad (16)$$

From Ref. 14, Eq. (16) becomes

$$I(\theta, \phi) = 2\beta(\bar{T}\pi ab)^2\left|\frac{J_1\{K[(a\theta)^2 + (b\phi)^2]^{1/2}\}}{K[(a\theta)^2 + (b\phi)^2]^{1/2}}\right|^2. \quad (17)$$

As in Eq. (5), the factor $\bar{T}\pi ab$ is the volume of a flattened elliptical cell (V_{cell}), and $2\beta V_{\mathrm{cell}}{}^2$ is the scattering intensity in the forward direction.

Equation (17) describes the scattering pattern of an ellipse with principal axes parallel to the x and the y axes in the scattering plane. To express the scattering pattern of an inclined ellipse as a function of Ω (see Fig. 2), i.e., the inclination angle of the ellipse's major axis with respect to the x axis, a change of coordinates is required:

$$\theta' = \theta\cos\Omega + \phi\sin\Omega,$$
$$\phi' = -\theta\sin\Omega + \phi\cos\Omega. \quad (18)$$

One chooses a fixed axis on the (θ, ϕ) plane, for example, $\phi = 0$, along which the scanning measurement of the diffraction pattern can be performed; inserting Eqs. (18) into Eq. (17) yields

$$I(\theta, \Omega) = 2\beta V_{\mathrm{cell}}{}^2\left[\frac{J_1[K\theta(a^2\cos^2\Omega + b^2\sin^2\Omega)^{1/2}]}{K\theta(a^2\cos^2\Omega + b^2\sin^2\Omega)^{1/2}}\right]^2. \quad (19)$$

To simplify Eq. (19), the approximation of Eq. (7) is used, yielding

$$I(\theta) = \frac{2\beta V_{\mathrm{cel}}{}^2}{\pi}\frac{1-\sin\{2K\theta[(b^2-a^2)\sin^2\Omega + a^2]\}^{1/2}}{\{K\theta[(b^2-a^2)\sin^2\Omega + a^2]^{1/2}\}^3}. \quad (20)$$

For brevity, the coefficient $2\beta V_{\mathrm{cell}}{}^2/\pi$ will be omitted from subsequent expressions.

The overall scattering pattern $II(\theta)$ of a homogeneous population of elliptic objects randomly oriented in the scattering plane would be composed of many such patterns [Eq. (20)], except that the angle Ω can vary between 0 and π.

With the same weighted Fourier transform as in Eq. (12), the spatial spectrum of such a population can be written as

$$II(\omega) = \Im\{I(\theta)(K\theta)^3\} = \left|\int_{-\infty}^{\infty}\int_0^{\pi} I(\Omega, \theta)p(\Omega)(K\theta)^3\exp(i\omega\theta)\mathrm{d}\Omega\mathrm{d}\theta\right|, \quad (21)$$

where $p(\Omega)$ is a general orientational distribution, which equals $1/2\pi$ in a randomly oriented population scatterer.

Inserting Eq. (20) into Eq. (21) yields

$$II(\omega) = \frac{1}{2\pi}\int_{-\infty}^{\infty}\int_{\Omega=0}^{\pi}\mathrm{d}\Omega\mathrm{d}\theta \times \frac{(1-\sin\{2K\theta[(b^2-a^2)\sin^2\Omega + a^2]^{1/2}\})\exp(i\omega\theta)}{[(b^2-a^2)\sin^2\Omega + a^2]^{3/2}}. \quad (22)$$

To allow us to evaluate this integral, a new variable γ is introduced:

$$\gamma = [(b^2-a^2)\sin^2\Omega + a^2]^{1/2},$$

where

$$\mathrm{d}\Omega = \frac{\gamma\mathrm{d}\gamma}{(\gamma^2-b^2)^{1/2}(a^2-\gamma^2)^{1/2}}. \quad (23)$$

Changing variables and the limits of integration gives us

$$II(\omega) = 2\left|\frac{\int_{-\infty}^{\infty}\int_a^b(\mathrm{d}\theta\mathrm{d}\gamma/\gamma^2)[1-\sin(2K\gamma\theta)]\exp(i\omega\theta)}{(\gamma^2-b^2)^{1/2}(a^2-\gamma^2)^{1/2}}\right|.$$

Integration over θ yields

$$II(\omega) = \times\left|\frac{\int_a^b(\mathrm{d}\gamma/\gamma^2)[2\delta(\omega) + \delta(\omega-2K\gamma) + \delta(\omega+2K\gamma)]}{(\gamma^2-b^2)^{1/2}(a^2-\gamma^2)^{1/2}}\right|. \quad (24)$$

Finally, considering only the positive values of ω in Eq. (24), one obtains

$$II(\omega) = 2C\delta(\omega) + \frac{(2K/\omega)^2 2K}{[\omega^2-(2Kb)^2]^{1/2}[(2Ka)^2-\omega^2]^{1/2}}, \quad (25)$$

where

$$C = \lim_{\epsilon\to 0}\int_{b+\epsilon}^{a-\epsilon}[(\gamma^2-b^2)^{1/2}a^2 - \gamma^2]^{1/2}\frac{\mathrm{d}\gamma}{\gamma^2}.$$

This result represents the parameters that one might extract from a Fourier transform of an optical diffraction pattern created by a population of elliptic objects. It contains a component at zero frequency, $2C\delta(\omega)$, and a more complicated continuous spectrum in the range $2Ka \le \omega \le 2Kb$. For a population of round objects with radius R, Eq. (25) predicts a spectrum with a single peak at $\omega \to 2KR$, and for elliptic objects it predicts a spectrum with two peaks, at $\omega = 2Ka$ and $\omega = 2Kb$, with an intermediate region.

The peak-height ratio (PHR) of such a spectrum is

calculated with a weighted power spectrum $S(\omega) \equiv II(\omega)\omega^2$.

$$\begin{aligned}\text{Ratio} &= \lim_{\Delta\omega\to 0}\left\{\frac{(S[\omega \to (2Ka - \Delta\omega)])}{S[\omega \to (2Kb + \Delta\omega)]}\right\} \\ &= \lim_{\Delta\omega\to 0}\left(\left\{\frac{[(2Kb + \Delta\omega)^2 - (2Kb)^2]^{1/2}}{[(2Ka - \Delta\omega)^2 - (2Kb)^2]^{1/2}}\right\}\right. \\ &\quad \left.\times\left\{\frac{[(2Ka)^2 - (2Kb - \Delta\omega)^2]^{1/2}}{[(2Ka)^2 - (2Ka - \Delta\omega)^2]^{1/2}}\right\}\right) \\ &= \left\{\frac{[(2Ka)^2 - (2Kb)^2]^{1/2}}{[(2Ka)^2 - (2Kb)^2]^{1/2}}\right\}\left\{\frac{(4Kb\Delta\omega)^{1/2}}{(4Ka\Delta\omega)^{1/2}}\right\} = \left(\frac{b}{a}\right)^{1/2}.\end{aligned} \tag{26}$$

It should be emphasized that this solution is valid only when the scatterer dimensions and shape are homogeneous.

D. Limitations on the Scattering Angle θ

The experimental assumption presented in Subsection 2.A limits the range of the scattering angle to be investigated to $\theta_{\min} \le \theta \le \theta_{\max}$, where $\theta_{\min} = (KR)^{-1}$ and $\theta_{\max} = (0.6\lambda/T)^{1/2}$. $II(\theta)$ is therefore modulated (subscript M) in the scattering plane by a rectangular window function $W(\theta)$, with a width of $\Delta\theta = \theta_{\max} - \theta_{\min}$, defined by

$$W(\theta) = \begin{Bmatrix}1 & |\theta| < \theta_{\max} \\ 0 & |\theta| > \theta_{\max}\end{Bmatrix}.$$

Thus

$$II_M(\theta) = II(\theta)W(\theta),$$

and the Fourier transform of the product is

$$\begin{aligned}\Im\{II_M(\theta)\} &= \Im\{II(\theta)W(\theta)\} \\ &= (1/2\pi)\Im\{II(\theta)\} * \Im\{W(\theta)\} \\ &= (1/2\pi)II(\omega) * \sin c(\omega\theta),\end{aligned} \tag{27}$$

where the symbol $*$ stands for convolution. This result indicates that both Eqs. (14) and (25) are spectrally broadened by $2\pi/\Delta\theta$, resulting in a loss of resolution. This holds for computer simulations as well as for experimental data analysis.

3. Materials and Methods

A. Polystyrene Bead Sample

Spherical polystyrene beads (CMPC, San Juan, Texas, special grade for Flow Cytometry Standard Corporation) of diameters 9.1 and 7.4 μm with a standard deviation of 0.2 μm were used to calibrate the optical system. The justification for the use of beads is as follows. The phase accumulated by wavelets going through a transparent disk is $(2\pi/\lambda)\Delta nT$ in relation to wavelets passing by it. Interference between these two sets of wavelets creates a diffraction pattern that reflects the diameter of the disk. The path length of rays within a spherical object is diverse and causes a phase difference among the rays, which depends on the distance of the rays from the central axis of the sphere and equals $(2\pi/\lambda)\Delta n\Delta T$, where ΔT is the local thickness of the sphere.

Two extreme cases should be noted. When Δn is small (as in cells suspended in phosphate-buffered saline), refraction is virtually null, and rays passing through the spherical object are effectively parallel, possessing a small phase difference, averaged as $(2\pi/\lambda)\Delta n\bar{T}$, where $\bar{T}$ is the effective thickness of the sphere. This approach is the basis for all the approximations in this paper (in addition to the fact that sedimentation causes cell flatness). On the other hand, when Δn is large (as for polystyrene beads in water), refraction is dominant, converging the rays into the object or within its vicinity with a wide variety of phase shifts. These phase shifts cause destructive interference among rays interacting with the spherical object, decreasing the part of the refracted wave in the forward direction. Thus the resulting scattering pattern will be affected mostly by the rays that do not go through the spherical object, but pass by it. This is similar to the diffraction forward pattern created by a blocking disk of the same diameter; thus the analysis of the diffraction pattern of beads can be used for calibration of living-cell measurements.

B. Cell Sample

Biological stimulation of living cells is associated with changes in their conformation and changes at the molecular level (e.g., membrane surface receptors). The latter are commonly monitored by fluorescent markers, but measurement can suffer from lack of specificity, labeling problems, dye release and leakage, autofluorescence, background (fluorescence and stray light), and above all limited duration because of labeling instability. To trace cell stimulation processes over long periods, free of the mentioned limitations, cellular conformations were monitored in this study by means of differential light scattering.

Granulosa follicle-stimulating hormone rounding-17 cells were obtained from Abraham Amsterdam of the Molecular Endocrinology Department, Weizmann Institute of Science, Rehovot, Israel. These cells have been shown[15] to change their morphology in the presence of follicle-stimulating hormone. For morphological examination by light scattering, cells were grown on a square cover glass (22 mm × 22 mm) in the presence of 5% fetal calf serum to avoid detachment of the cells during their fixation, obtained with 2.7% glutaraldehyde in phosphate-buffered saline (pH = 7.4) for 30 min at 24 °C. The cover glasses loaded with cells were then washed several times with this saline, until free of fixative, and were mounted with elvanol on a supporting microscope glass slide.

C. Measurement System

The experimental instrumentation, presented schematically in Fig. 3, includes a low-power He–Ne laser (1 mW). Scattered light is collected along an arclike

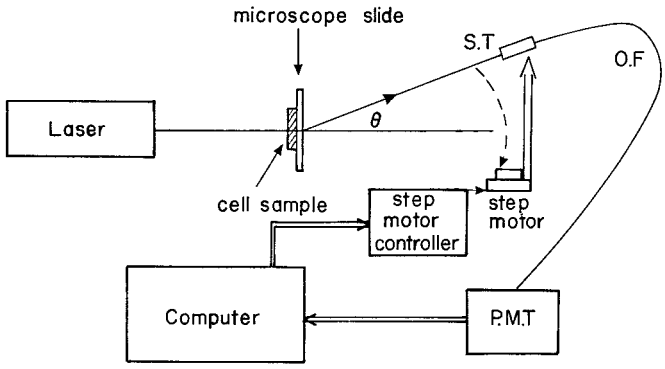

Fig. 3. Measuring system arrangement. A He–Ne laser beam, $\lambda = 632$ μm, illuminates a sample cell population attached to a microscope slide. The diffraction pattern is scanned along an arclike trajectory (S.T) by a movable optical fiber (O.F), which transmits the light to a photomultiplier tube (P.M.T). The successive signals are analyzed by the computer.

trajectory with an optical fiber (diameter $D = 400$ μm) connected to a photomultiplier tube (Hamamatsu R928).

The mechanical system that holds and positions the fiber-optics line is connected to a stage driven along an arc trajectory by a computer-controlled step motor (Warner Electric/Superior Electric, Model SLO-SYN, Serial MO61 FCO2E, Michigan), which permits accurate positioning and scan duration.

The electronic system consists of a differential, 12-bit, analog-to-digital card. The electronic signals generated by the photomultiplier tube are passed to the card together with an offset bias voltage to nullify noise and background. Software packages written in C provide digital-to-analog conversion and data acquisition as well as calculation utilities, file management, and stage control.

D. Simulation of the Scattering Pattern

A computer program was used to produce a simulated scattering pattern created by a randomly oriented and located population of 1500 identical elliptical objects. For that purpose a standard Fourier procedure was applied to a spatial configuration containing the object population. The black areas that indicate full destructive interference obtained by the program are illustrated in Fig. 4.

E. Determination of Morphological Parameters

The simulated measured scattering intensity pattern, which is proportional to the square of the absolute value of the field, was subjected to an analysis procedure which was, essentially, a weighted inverse Fourier transform. In addition to some windowing treatment, a fast Fourier transform was used.

We obtain the simulated measured data by sampling the simulated intensity pattern over the region $\theta_{\min} \le \theta \le \theta_{\max}$ ($\theta_{\min}$ and $\theta_{\max}$ are defined in Subsection 2.D). In terms of the sampling interval $\Delta\theta = \theta_{\max} - \theta_{\min}$, the sampled intensity pattern is written as a data vector of the form

$$I_P = I\left(\theta_{\min} + \frac{p\Delta\theta}{P}\right),$$

where $p = 0, 1 \ldots, (P - 1)$ is the index number of a sampled point and P is the total number of sampling points, which should obey Nyquist's condition[16] $P \ge (2D/\lambda)\Delta\theta$.

To compensate for the decrease of $I(\theta)$ given in Eq. (20), the vector I_P is weighted according to Eq. (21) by $c_P = (\theta_{\min} + p\Delta\theta/P)^3$. The resulting vector $G_p \equiv I_p c_p$ is then subjected to the fast Fourier transform procedure so that a discrete spectral vector $\tilde{G}_q$, having P frequency components, is created. Compensating again for the ω^{-2} decrease, as is implied by Eq. (25), $\tilde{G}_q$ is multiplied by a vector $\alpha_q = q^2$, so that $\tilde{S}_q = \tilde{G}_q q^2$.

Then q_0 (the index of $\tilde{S}_q$ at its maximum point) is rescaled in the frequency axis to represent the object size D in micrometers. Rescaling takes into account the wavelength of the incident radiation and the angular range of the scattering data used in the fast Fourier transform process so that $D\ (\mu\text{m}) = \tilde{q}_0(\lambda/\Delta\theta)$.

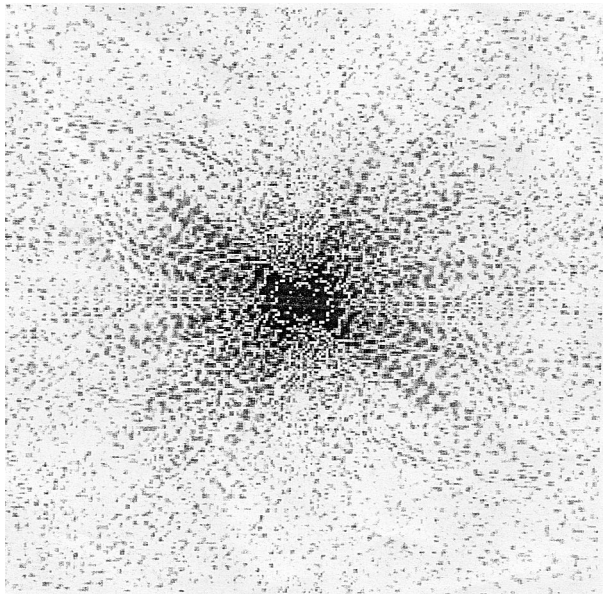

Fig. 4. Scattering pattern of 1,500 optical scatterers obtained by computer simulation ($a/b = 3$). The screen angular dimensions are approximately 0.8 rad. Black areas, full constructive interference; white regions, full destructive interference; gray areas, intermediate levels of interference.

4. Results and Discussion

A. Computer Simulation of Diffraction Pattern Created by a Population of Elliptical Objects

To confirm the validity of Eq. (25), a simulated experiment was conducted in which a population of elliptic scatterers was illuminated by a coherent laser beam whose wavelength was ~1 order of magnitude smaller than the size of the single scatterer.

The diffraction pattern was created by numerical calculation[17] of the integral of Eq. (15). This was done by summing the phasors which correspond to each element within the total aperture function $T_{AP}(x, y)$ on the plane $z = 0$ (Fig. 1):

$$E(p, q) \rightarrow \left| \int_{-x_0/2}^{x_0/2} \int_{-y_0/2}^{y_0/2} T_{AP}(x, y) \exp(iKx\theta) \times \exp(iKy\theta) dx dy \right|^2 \rightarrow \lim_{N,M\rightarrow\infty} \sum_{n=0}^{N-1} \sum_{m=0}^{M-1} T_{AP}(n, m) \times \exp[i(2\pi/N)np] \exp[i(2\pi/M)mq], \quad (28)$$

where $T_{AP}(x, y)$ represents the total aperture function of the entire population, N and M are the number of pixels in the x and y image axes, respectively, n and m are the indices of the x and y directions on an object plane $z = 0$, and p and q are the spatial frequencies in the x' and y' directions, respectively, on the scattering plane $z = z_S$ (Fig. 1). In this way, the simulated scattering pattern is computed for the plane $z = z_S$ (Fig. 2). It is necessary to find the appropriate scaling for a realistic experiment. Comparing the corresponding exponents of the discrete and the continuous expressions in relation (28) gives

$$i(2\pi/N)np = i(2\pi/\lambda)X\theta. \quad (29)$$

Replacing X with the discrete expression $(L_0/N)n$, where L_0 is the size of the illuminated region, and inserting the result into Eq. (29) gives us

$$i(2\pi/N)np = i(2\pi/\lambda)(L_0/N)n\theta. \quad (30)$$

In evaluating the number of sampling points needed for adequate simulation, we note that the last point of sampling would be at a location P corresponding to $\theta = \theta_{max}$ (see Subsection 2.D). Thus, substituting θ_{max} into Eq. (30) gives Eq. (31):

$$P = (L_0/\lambda)\theta_{max} \quad (31)$$

where (L_0/λ) is the scaling factor for simulation, and the index of the last meaningful pixel in the simulation is determined by our rounding off $(L_0/\lambda)\theta_{max}$. Under the typical experimental conditions, $\lambda = 0.6328$ μm, $L_0 \sim 500$ μm, $R \approx 10$ μm, and $T \approx 5$ μm, one finds that $(L_0/\lambda) \approx 1000$, $\theta_{max} \approx 0.3$ rad, and $P \approx 300$. Similar considerations hold for the index q.

A graphical representation of the scattering pattern is shown in Fig. 4. This particular image was created by a discrete Fourier transform applied to a spatial configuration of 1500 elliptical objects having a principal axes ratio of $a/b = 3$.

Marked differences exist between a pattern such as that given in Fig. 4 and a conventionally analyzed scattering pattern. The most obvious difference is the absence of the usual circular interference fringes, which is an understandable result of the reduced symmetry of the single elliptic scattering object when compared to that of a sphere.

B. Windowing and Weighting

The simulated scattering pattern $I(p, q) = 1/2|E(p, q)|^2$, obtained by application of relation (28), is truncated to eliminate angles that are nonphysical according to Eq. (31). The central horizontal vector is selected from the remaining matrix $I(p, q)$, and a weighted inverse Fourier transform is performed as required in Eq. (21).

C. Spectrum Interpretation

The spectrum itself is predicted to be a decreasing function of the form ω^{-2}. To observe different spectra in a convenient manner, compensation for the decrease is made by defining $S(\omega) = II(\omega)\omega^2$ as the weighted spectrum. Using this analysis procedure, four populations of elliptic objects were chosen, to which weighted Fourier spectra $S(\omega)$ were computed and compared with theory. Theoretical spectra are plotted by use of Eq. (25). Both theoretical and simulated results are presented graphically in Fig. 5.

In each case the minor axis was fixed at $b = 5$ μm, whereas the major axis was changed from $a = 6$ μm to $a = 10, 15, 20$ μm. As can be seen, the theoretical curves (dashed curves) are in good agreement with the simulation curves (solid curves). However, significant fluctuations are present, mostly in the lower panels of Fig. 5. This is due to the fact that a given interval in frequency axis represents a smaller fraction of the overall population as the major axis of the scatterer is enlarged. This fact and the finite number of scatterers gives rise to the inevitable fluctuations (Figs. 5c and 5d). Turning to the peaks in Fig. 5, good agreement is apparent between theory and simulation regarding their locations and PHR (See Table 1).

5. Experimental Results

A. Spherical Objects

We calibrated the optical setup and analysis procedure by scanning the diffraction patterns obtained from four populations of spherical polystyrene beads with diameters of 9.1, 7.4, 6.4, and 5 μm and a standard deviation of 0.2 μm. Although optically and geometrically different from living cells, these beads may serve as reasonable calibrators, as was shown in Subsection 3.A. This procedure is justified because the light scattered to small angles by a bead is diffractive[12] owing to its relatively large Δn. This implies that the scattering pattern of a bead is affected mainly by its maximum cross section in a way similar to that of an absorbing disc. After the spatial frequency for each bead population was obtained, a calibration curve was constructed that permitted transformation from spatial frequency to size in micrometers.

B. Morphological Appearance of Cells

The follicle stimulating hormone that stimulated the cyclic adenosin monophosphate-stimulated response in the cells was correlated with their morphological appearance. Specimens were inspected and photo-

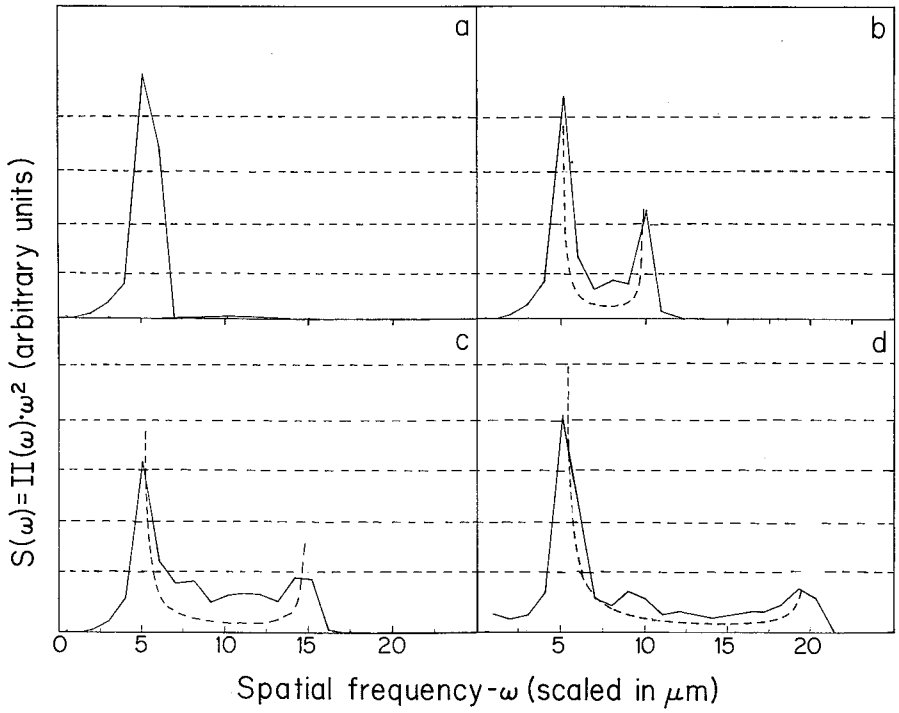

Fig. 5. Power spectra of populations of elliptic scatterers as obtained by computer simulation (solid curves) and theory (dashed curves). The abscissa is the weighted power spectrum $S(\omega) = \Pi(\omega)\omega^2$, and the ordinate is the spatial frequency (ω) axis. Results obtained for $\epsilon = a/b = 6/5, 2, 3, 4$ are presented in a, b, c, d, respectively. For a numerical comparison, see Table 1. Note that there is no dashed curve for a because it is almost spherical (homogeneous); the result is a δ function, which is just a point on the graph.

graphed with a phase-contrast microscope (Zeiss Photomicroscope III, Fig. 6) and subsequently analyzed on the scattering apparatus. Mounted specimens were kept at 4 and 24 °C for several months without any detectable change in cell morphology. Following incubation with 0.24 nM of follicle-stimulating hormone, cells remained partially elongated (Fig. 6A), whereas 2.4 nM caused significant rounding (Fig. 6B). These morphological changes include more than 95% of the cell population and are entirely preserved subsequent to glutaraldehyde fixation, performed at the end of the above hormone-stimulation period. No rounding of cells was observed when they were stimulated with ovine lutenizing hormone or human chronionic gonadotropin at comparable concentrations. The quantification of such spectra is currently under investigation.

In Fig. 7 the spectrum has a narrower bimodal distribution located at frequencies corresponding to 10–20 μm. This spectrum—the outcome of the scattering pattern of the sample shown in Fig. 6A—shows good agreement with the theory developed for elliptic scatters. At higher follicle-stimulating hormone concentrations, where most cells are rounded (Fig. 6), the corresponding spectrum has only one dominant peak near $\omega = 10$ μm (Fig. 7b), which is indeed the mean diameter of the rounded cell. The theoretical PHR for such objects is ~0.6; the measured ratio is ~0.45, which may be because the cells are not exactly elliptical.

Table 1. Comparison between Theoretical and Simulated PHR

ϵ (a/b)	Predicted PHR $[(b/a)^{1/2}]$	Simulated PHR
1.11	0.95	0.93
2	0.71	0.70
3	0.58	0.57
4	0.5	0.48

6. Conclusions

In this study the Fourier analysis of light scattered by a population of elliptic scatterers has been discussed theoretically and investigated experimentally for what is the first time to the best of our knowledge.

It should be noted that the results shown here were obtained under three assumptions:

(a) The investigated object is partially flat.

(b) Assumption (a) is justified by the fact that the multiplication of the measured spectrum $I(q)$ by the factor q^2 (see Subsection 3.E) enhances the higher-spatial-frequency content in the scattering pattern, which is associated with large dimensions. By the same reasoning, internal structure that is characterized by small dimensions corresponds to low spatial frequencies and is thus not likely to affect the calculated size of the object.

(c) The population of scatterers is homogeneous.

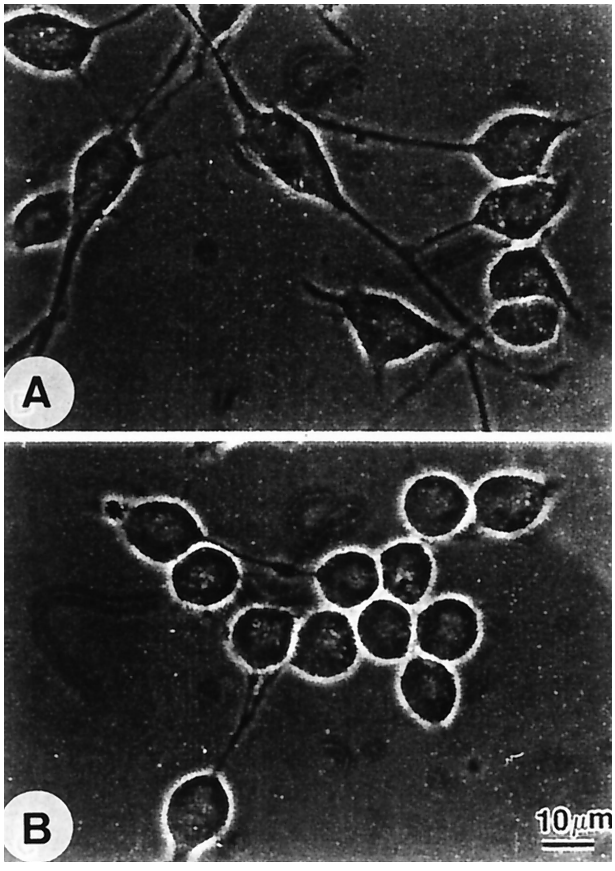

Fig. 6. Morphological changes in granulosa follicle-stimulating hormone rounding-17 cells following follicle sensitive hormone stimulation. Phase-contrast images of cells stimulated for 24 h with, A, 0.24 nM follicle-stimulating hormone or, B, 2.4 nm of the same hormone.

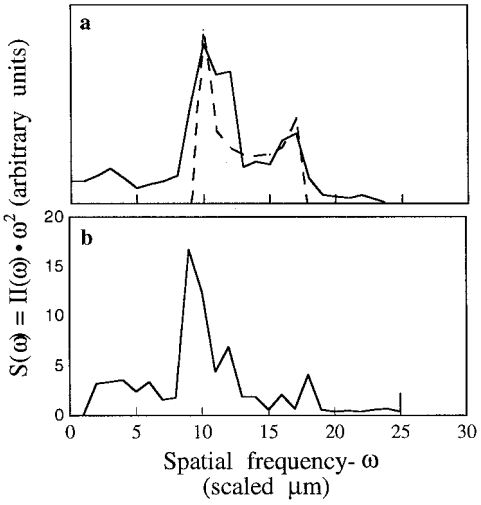

Fig. 7. Effect of follicle-stimulating hormone concentrations on weighted power spectra $S(\omega) = II(\omega)\omega^2$. The theoretical (dashed) curve expected for the cells according to their appearance in the light microscope, and $S(\omega)$, which we calculated by subjecting the real scattering light intensity patterns to a Fourier transform and smoothing it by using a spline procedure (solid curve) of two cell samples, incubated for 24 h with, a, 0.24 nm or, b, 2.4 nM of this hormone, and subsequently fixed on a microscope slide on which they were cultivated. Note that there is no dashed curve for b, for the same reason as given in the caption for Fig. 5a.

While the first two are realistic assumptions, the latter may not be, and one should reconsider $II(\omega)$ for a distribution of scatterer geometries, a treatment not included in this study.

Subject to the above assumptions, an interesting result is obtained from the power spectrum, according to which the PHR is given by the ratios of the square roots of their locations:

$$\text{Ratio} \equiv \lim_{\Delta\omega \to 0} s \frac{S[\omega \to (2Ka - \Delta\omega)]}{S[\omega \to (2Kb + \Delta\omega)]} = \left(\frac{b}{a}\right)^{1/2}.$$

Hence elongated scatterers have a characteristic spectrum, a result predicted by theory, confirmed by computer simulation, and in reasonable agreement with experimental results obtained from tracing the rounding process of elongated granulosa follicle-stimulating hormone rounding-17 cells. The model developed for elliptic scattering was also examined within the limits of the case of spherical scatterers and yielded the expected single-peak spectrum.

In this study formulation, simulation methods, and a device have been developed and applied to produce an integrated profile of the size and shape distribution of a tested population of cells. This was achieved by means of a spatial frequency analysis. Analyzing the angular distribution of the scattered light intensity by Fourier transformation can thus yield a specific inverse Fourier transform pattern that can be correlated to the size and shape distribution for the entire cell population.

Numerous biological responses in living cells are associated with a dramatic change of cell shape.[18–20] Most common are those systems in which a hormone or neurotransmitter binds to a specific receptor located on the cell surface, leading to activation of the enzyme adenylate cyclase and to cyclic adenosine monophosphate accumulation. The latter can subsequently lead to changes in the organization of the cytoskeleton and changes in cell shape and size.[18] This is the case in gonadotropins, hormones, thyrotropin-stimulating hormone, glucagon and the β adrenergic receptors. The methodology (method, formulation, and apparatus) described in this study can lend itself to translating hormonal response of cells to changes in physical parameters such as spatial frequency of the diffraction pattern, which is a reflection of morphological changes.[6] Furthermore, analyzing the entire cell population may yield important information about the uniformity of the hormonal response over the entire cell population.

The results indicate that Fourier analysis may be applied quantitatively to trace structural changes that occur during biological processes. Light scattering experiments on biological samples are currently being carried out, with the extension of the method, for the investigation of a variety of scatterer geometries.

References

1. I. A. Schafer, A. M. Jamieson, M. Petrelli, B. J. Price, and G. C. Salzman, "Multiangle light scattering flow photometry of cultured human fibroblasts. Comparison of normal cells with a mutant cell line containing cytoplasmic inclusions," J. Histochem. Cytochem. **27,** 359–365 (1979).
2. G. C. Salzman, P. F. Mullaney, and B. J. Price, "Light-scattering approaches to cell characterization," in *Flow Cytometry and Sorting*, M. R. Melamed, P. F. Mullaney, and M. R. Mendelsohn, eds. (Wiley, New York, 1979), pp. 108–124.
3. G. C. Salzman, J. M. Crowell, C. A. Goad, K. M. Hansen, R. D. Hiebert, P. M. LaBauve, J. C. Martin, M. Ingram, and P. F. Mullaney, "A flow-system multiangle light scattering instrument for cell characterization," Clin. Chem. **21,** 1297–1304 (1975).
4. G. Seger, M. Achatz, W. Heinze, and F. Sinsel, "Quantitative extraction of morphological cell parameters from the diffraction pattern," J. Histochem. Cytochem. **25,** 707–718 (1977).
5. B. Turke, G. Seger, M. Achatz, and V. S. Werner, "Fourier optical approach to the extraction of morphological parameters from the diffraction pattern of biological cells," Appl. Opt. **17,** 2754–2761 (1978).
6. D. E. Burger, J. H. Jett, and P. F. Mullaney, "Extraction of morphological features from biological models and cells by Fourier analysis of static light scatter measurements," Cytometry **2,** 327–336 (1982).
7. A. Brunsting and P. F. Mullaney, "Light scattering from coated spheres: models for biological cells," Appl. Opt. **11,** 675–680 (1972).
8. S. Asano and M. Sato, "Light scattering by randomly oriented spheroidal particles," Appl. Opt. **19,** 972–974 (1980).
9. R. A. Dobbins and C. M. Megaridis, "Absorption and scattering of light by polydisperse aggregates," Appl. Opt. **30,** 4747–4754 (1991).
10. S. Asano and G. Yamamoto, "Light scattering by a spheroidal particle," Appl. Opt. **14,** 29–49 (1975).
11. J. B. Riley and Y. C. Agrawal, "Sampling and inversion of data in diffraction particle sizing," Appl. Opt. **30,** 4800–4817 (1991).
12. S. Evans, "Comparison of the diffraction theory of image formation with the three-dimensional, first Born scattering approximation in lens systems," Opt. Commun. **2,** 317–320 (1970).
13. S. D. Coston and N. George, "Particle sizing by inversion of the optical transform pattern," Appl. Opt. **30,** 4785–4794 (1991).
14. I. S. Gradshteyn and I. M. Ryzhik, ed., *Tables of Integrals, Series and Products*, 5th ed., (Academic, New York, 1965), p. 954.
15. I. Keren-Tal, A. Dantes, R. Sprengel, and A. Amsterdam, "Establishment of steroidiogenic granulosa cell lines expressing follicle stimulating hormone receptors," Mol. Cell Endocrinol. **95,** R1–R10 (1993).
16. J. B. Riaey and Y. C. Agrawal, "Sampling and inversion of data in diffraction particle sizing," Appl. Opt. **30,** 4800–4816 (1991).
17. A. Papoulis, *Signal Analysis* (McGraw-Hill, New York, 1986), p. 79.
18. A. Amsterdam and D. Aharoni, "Plasticity of cell organization during differentiation of normal and oncogene transformed granulosa cells," Microsc. Res. Tech. **27,** 108–124 (1994).
19. A. Brunsting and P. F. Mullaney, "Differential light scattering from spherical mammalian cells," Biophys. J. **14,** 439–453.
20. M. Zohar and Y. Salomon, "Melanocortins stimulate proliferation and induce morphological changes in cultured rat astrocytes by distinct transducing mechanisms," Brain Res. **576,** 49–58 (1992).